Chapter 2

Ultra-Sensitive Surface Plasmon Resonance Detection by Colocalized 3D Plasmonic Nanogap Arrays

Wonju Lee, Taehwang Son, Changhun Lee, Yongjin Oh, and Donghyun Kim

Abstract

Ultra-sensitive detection based on surface plasmon resonance (SPR) was investigated using 3D nanogap arrays for colocalization of target molecular distribution and localized plasmon wave in the near-field. Colocalization was performed by oblique deposition of a dielectric mask layer to create nanogap at the side of circular and triangular nanoaperture, where fields localized by surface plasmon localization coincide with the spatial distribution of target molecular interactions. The feasibility of ultra-sensitivity was experimentally verified by measuring DNA hybridization. Triangular nanopattern provided an optimum to achieve highly amplified angular shifts and led to enhanced detection sensitivity on the order of 1 fg/mm^2 in terms of molecular binding capacity. We confirmed improvement of SPR sensitivity by three orders of magnitude, compared with conventional SPR sensors, using 3D plasmonic nanogap arrays.

Key words Surface plasmon resonance, Localized surface plasmon resonance, Surface plasmon resonance detection, Nanogap arrays, Nanoapertures, Colocalization, DNA hybridization

1 Introduction

In recent years, diverse optical techniques have attracted tremendous interests for ultra-sensitive real-time detection of various phenomena involving biomolecular interactions. Most of these techniques have been based on fluorescence. Fluorescence-based sensing, however, suffers from fluorescence interference or chemotoxicity issues. In contrast, surface plasmon resonance (SPR) biosensing has been widely investigated as a representative label-free technique, by which specific molecular interactions can be monitored in real time and kinetic characteristics related to molecular binding are conveniently measured on a quantitative basis.

Surface plasmon (SP) is a collective logitudinal oscillation of electrons existing at the metal/dielectric interface. The oscillation of electron can be coupled with a TM-polarized incident light.

Avraham Rasooly and Ben Prickril (eds.), *Biosensors and Biodetection: Methods and Protocols Volume 1: Optical-Based Detectors*, Methods in Molecular Biology, vol. 1571, DOI 10.1007/978-1-4939-6848-0_2,

By tuning angle of incidence or incident wavelength, the momentum matching condition between incident light and SP can be satisfied. At resonance, due to energy transfer from incident light to a longitudinal surface wave, a narrow dip in the reflection characteristics is observed with respect to wavelength or angle of incidence. A small change of dielectric medium refractive index induced from a biochemical interaction affects momentum matching condition, followed by the shift of resonance dip in the reflection characteristics [1].

Despite broad uses of SPR sensors, conventional SPR sensors have relatively poor detection limit on the order of 1 pg/mm^2 in binding capacity [2]. As an optical sensing technique other than SPR, metal nanoparticle-based surface-enhanced Raman scattering and microresonator-based whispering gallery modes have emerged for ultra-sensitive label-free detection [3, 4].

In this chapter, we describe self-aligned colocalization using three-dimensional plasmonic nanogap arrays for ultra-sensitive SPR biosensors [5]. Note that colocalization indicates the spatial overlap between the area of localized electromagnetic field and molecular interaction. Colocalization is preferred in terms of sensitivity enhancement per molecule, because much smaller number of molecules are involved at the interaction. In previous studies, use of plasmonic nanostructures was investigated to localize SP and evanescent near-field to enhance detection sensitivity [6, 7]. Random and periodic nanostructure was also employed for specific and nonspecific detection based on enhanced surface plasmon resonance [8, 9]. It was also shown that when biomolecules are spatially aligned for colocalization with the localized field that is defined by 2D linear nanopattern arrays, SPR signals can be effectively amplified, which leads to efficient improvement of detection sensitivity [10–12]. Moreover, theoretical investigation of nonspecific, noncolocalized, and colocalized detection models was performed based on silver nanoislands, which confirmed possibility of further amplification of optical signature [13]. Meanwhile, SPR sensor characteristics using grapheme-related materials were also studied [14, 15].

Here, we describe use of 3D plasmonic nanogap arrays, illustrated in a schematic diagram of Fig. 1, for colocalized detection of bio-interactions of target molecules to achieve even more dramatic enhancement of sensitivity in SPR biosensors. In particular, circular and triangular nanoholes were developed lithographically and 3D nanogaps were then formed for colocalization by the shadowing of obliquely evaporated dielectric mask layer on the metallic nanostructures. This enables target molecules to directly access the underlying metal film. Oblique evaporation was previously used to fabricate molecular electronic devices based on nanoscale gap structures [16]. Since localized near-field is formed at the ridge of the nanostructure, localized fields and nanogap where target

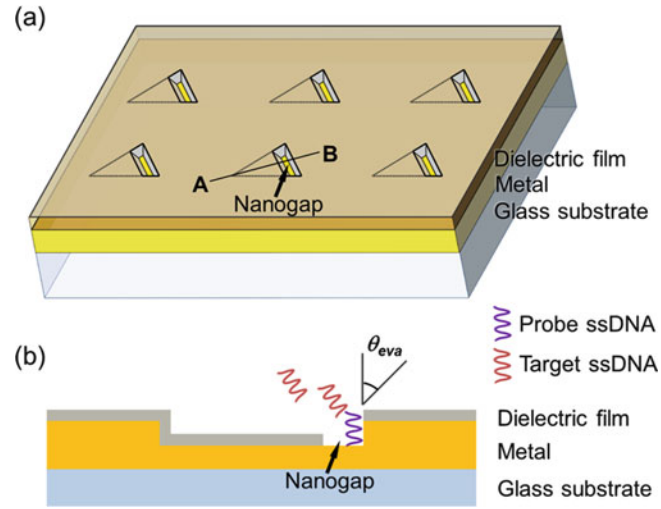

Fig. 1 (**a**) Schematic illustration of 3D triangular nanogap aperture arrays that may be produced by oblique evaporation for colocalized biomolecular interaction. (**b**) Lateral profile across the *solid line* (*A*–*B*) in (**a**)

molecules can bind are self-aligned for colocalization. 3D plasmonic nanostructures induce colocalization area to be much smaller than what 2D linear grating patterns may produce. Therefore, detection of much weaker interactions and/or those involve a smaller number of molecules would be feasible, which allows extreme sensitivity enhancement in SPR sensing.

2 Materials

2.1 Nanogap Fabrication

1. A glass substrate (SF10) with a 2-nm-thick chromium adhesion layer and a 40-nm-thick gold film.
2. Electron beam (VEGA II LSH; TESCAN, Brno, Czech).
3. Scanning electron microscope (Elphy Quantum; Raith, Dortmund, Germany).
4. A polymethylmethacrylate (PMMA) photoresist (AR-N 7520.18; ALLRESIST, Strausberg, Germany).
5. Spin-coater (ACE-200; DONG AH Trade Corp, Seoul, Korea).
6. A dielectric mask layer using ITO or SiO_2.
7. Developer (AR 300-47; ALLRESIST, Strausberg, Germany).
8. Remover (AR 300-70; ALLRESIST, Strausberg, Germany).

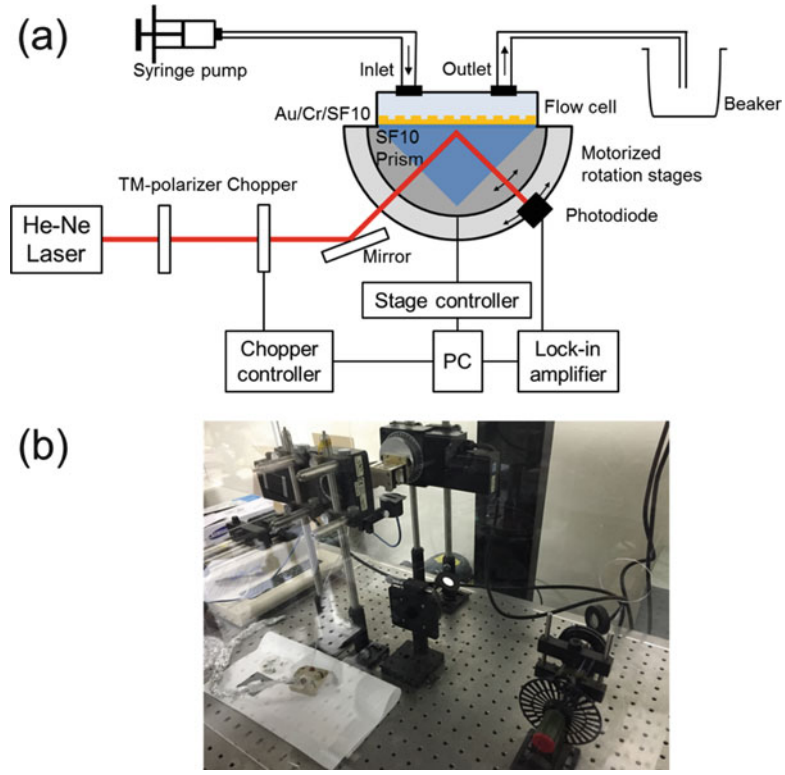

Fig. 2 (**a**) Schematics of optical setup for a SPR sensor based on colocalization using plasmonic nanogap arrays and (**b**) photograph of the experimental setup

2.2 Optical Setup

A schematic illustration of the optical setup for colocalized SPR detection is presented in Fig. 2 (*see* **Note 1**).

1. He-Ne laser (36 mW, $\lambda = 632.8$ nm, Nominal beam diameter: 650 μm; Melles-Griot, Carlsbad, CA).
2. Glan-Thompson Linear Polarizer (Thorlabs, Inc., Newton, NJ).
3. Chopper and controller (SR540; Stanford Research Systems, Sunnyvale, CA).
4. Two concentric motorized rotation stages (URS75PP and ESP330; Newport, Irvine, CA) (*see* **Note 2**).
5. Low-noise lock-in amplifier (Model SR830; Stanford Research Systems, Sunnyvale, CA).
6. A p-i-n photodiode (818-UV; Newport, Irvine, CA).
7. Lab ViewLabVIEW (National Instruments, Austin, TX).
8. Index-matching gel ($n = 1.725$; Cargille Laboratories, Cedar Grove, NJ).

2.3 DNA Preparation

1. HPLC purified 24-mer sequence length capture probe and target oligonucleotides (IDT, Coralville, IA).
2. The sequence of single-stranded probe DNA (p-DNA) was 5′-TTT TTT CGG TAT GCA TGC CAT GGC-3 modified with thiol at 5′.
3. The sequence of single-stranded target DNA (t-DNA) was 5′-GCC ATG GCA TGC ATA CCG AAA AAA-3′.
4. Plasma cleaner (Harrick Scientific Products, Pleasantville, NY).
5. Micropump (KD Scientific, Holliston, MA).
6. Acetone (1009-4404; DAEJUNG CHEMICAL & METALS CO., Siheung, Korea).
7. Phosphate Buffered Saline (PBS) buffer (pH = 7.4, BP3991; Fisher Scientific, Pittsburgh, PA).

3 Methods

3.1 Nanogap Fabrication

To make linear nanograting-based 2D nanogap arrays, the overall fabrication steps are explained below.

1. A 40-nm-thick gold film was evaporated on an SF10 glass substrate with a 2-nm-thick chromium adhesion layer.
2. Nanograting array patterns were defined by electron beam (e-beam) lithography using PMMA photoresist that was spin-coated on the gold film.
3. Metallic nanograting arrays were transferred by a lift-off process after gold evaporation (*see* Fig. 3a).
4. 2D nanogap arrays were created on nanograting arrays by oblique evaporation of a dielectric mask layer using ITO or SiO_2 (*see* Fig. 3b).

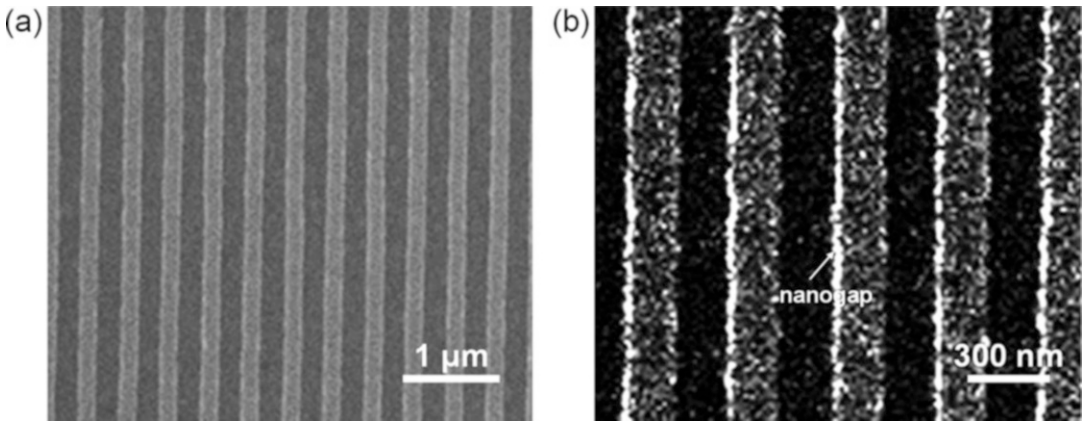

Fig. 3 (**a**) SEM image of fabricated linear nanograting arrays and (**b**) magnified image of 2D nanogap arrays

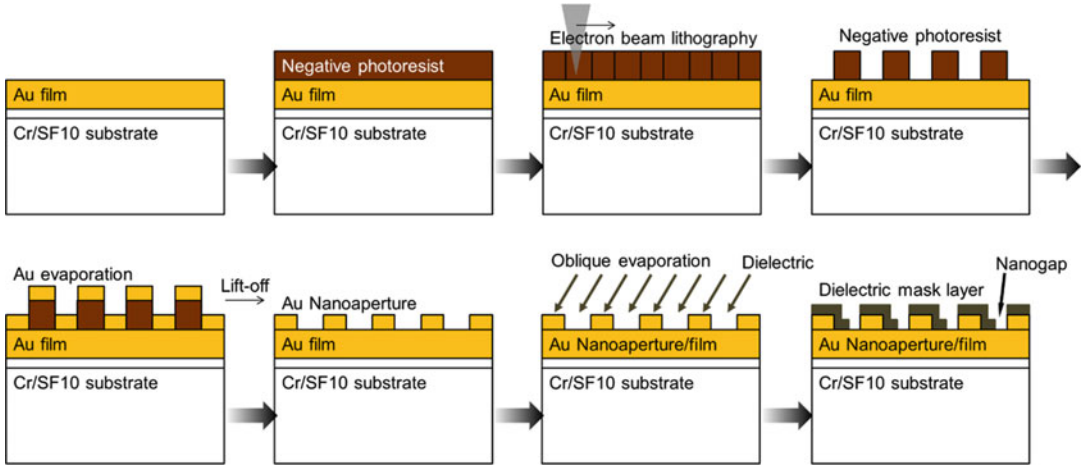

Fig. 4 Fabrication procedure to implement 3D plasmonic nanogap arrays

To create 3D nanogap arrays, the overall fabrication process is presented in Fig. 4.

1. A 40-nm gold film was evaporated on an SF10 glass with a 2-nm chromium adhesion layer.
2. Circular and triangular nanostructures with a 2-μm array period and an aperture size of 600 nm were defined by electron beam lithography.
3. 20-nm-thick nanohole arrays were formed after a lift-off process that involves e-beam lithography, evaporation of gold, and removal of polymer resist.
4. 5-nm-thick ITO layer was obliquely deposited with the deposition angle varied at 30°, 45°, and 60° to adjust the gap area differently (*see* **Note 3**).

3.2 Optical Setup

A He-Ne laser beam (36 mW, $\lambda = 632.8$ nm, nominal beam diameter: 650 μm, Melles-Griot, Carlsbad, CA) is TM-polarized by linear polarizer and temporally modulated by optical chopper (SR540; Stanford Research Systems, Sunnyvale, CA), which alters the state of light on and off at a specific frequency. The chopping frequency is used as the reference input of a lock-in amplifier composed with usually set to 0.6 kHz lock-in amplifier and feedback system. Among the signals captured at a photodiode, noise signal at frequency other than the chopping can be removed. Two motorized rotation stages (URS75PP; Newport, Irvine, CA) are employed; one is for rotating a prism on which a plasmonic nanostructured sample is located, and the other is for rotating the photodiode to keep laser alignment to photodiode. The angle of the stage on which the nanostructure sample located can be corrected by using the calibration constant and the other stage with the

photodiode follows the former stage. The nanostructured sample is located on the SF10 prism with index matching gel ($n = 1.725$; Cargille Laboratories, Cedar Grove, NJ), and covered with flow cell system head. Using one motor controller (ESP330, Newport), two stages are controlled at the same time with a minimum angle increment of 0.0002°, uni-directional repeatability of 0.001°, absolute accuracy of ±0.008°. A p-i-n photodiode (818-UV, Newport) is used to detect refractance change by the angle scanning. The value measured by the diode is used as input for the feedback system of lock-in amplifier. Therefore, the signal from photodiode is noise removed due to the phase-sensitive detection. The stage and chopper controller are connected to PC and controlled by LabVIEW, so whole system is fully automated.

3.3 Estimation of Colocalization Areas

3.3.1 2D Nanogap Production

A 2D nanogap area $G_{\Lambda,2D}$ produced by linear nanograting per unit grating length with the thickness d_g can be calculated as

$$G_{\Lambda,2D} = d_g(1 + \tan\theta_{eva}) \quad (1)$$

where θ_{eva} is the oblique evaporation angle (*see* Fig. 1b) in Eq. 1, the first term d_g and the second term $d_g \tan\theta_{eva}$ come from vertical nanograting edge and horizontal surface which are not evaporated with dielectric, respectively. For example, when the nanograting with $d_g = 20$ nm and $\theta_{eva} = 30°$ produces a nanogap with an area of 31.56 nm times the grating length.

3.3.2 Nanogap Reduction of the Colocalization Area

3D nanoaperture arrays can reduce the colocalization area, in which target molecular binding overlaps with localized fields to amplify optical signatures of the target interaction. A 3D nanogap area defined by an equi-triangular aperture with a side length (L) is calculated as

$$G_{\Lambda,3D} = Ld_g \times \left[(1 + \tan\theta_{eva}) + \frac{d_g \tan\theta_{eva}}{\sqrt{3}L}(2 - \tan\theta_{eva})\right] \quad (2)$$

where the direction of oblique evaporation is parallel to a side of a triangular pattern. The first term Ld_g represents the area open to the side, while the second term $Ld_g \tan\theta_{eva}$ is the area formed at nanogap surface. The last term in Eq. 2 is the correction due to the triangular shape. If L is much longer than d_g, the above equation can be simplified as

$$G_{\Lambda,3D} \approx Ld_g \times (1 + \tan\theta_{eva}). \quad (3)$$

In the case of using circular nanoholes, the nanogap area with a nanohole diameter (ϕ) is changed to

$$G_{\Lambda,3D} \approx \frac{\pi\phi}{2} d_g \times \left(1 + \frac{1}{2}\tan\theta_{eva}\right). \quad (4)$$

Using 3D nanogap arrays, the number of molecular interactions can be adjusted by changing the size to period ratio L/Λ.

3.4 Numerical Studies

In this section, the effectiveness of colocalization is evaluated from numerically calculated near-field distribution and the experimentally determined nanogap area. Electromagnetic field distribution at the nanogap was theoretically calculated based on rigorous coupled wave analysis (RSoft DiffractMOD™). Numerical calculation with DNA molecules can be done as below.

1. DNA molecules are assumed to be uniformly distributed on the nanogap.
2. The thickenss of hybridized DNA layers is modeled to 8.16 nm, which corresponds to the length of oligonucleotides.
3. The refractive indices of ssDNA and dsDNA are set to 1.449 and 1.517 [17].

As shown in Fig. 5, it is clear that fields are highly localized at nanogap. The presence of side lobe peaks was also observed on the opposite side of nanogaps, which cannot be neglected compared with the main peaks of localized fields. The suppression ratio, defined as the intensity ratio of the main peak to that of side lobe, in circular and triangular nanopatterns was estimated to be 2.3–2.5 dB. In the case of colocalization, optical signature detected at the main peak can be dominant because of spatial selectivity of

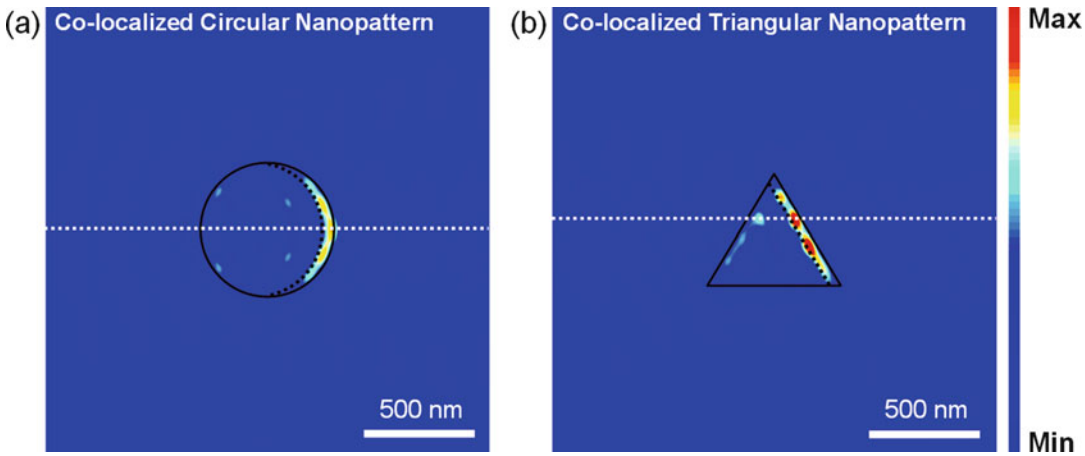

Fig. 5 Numerically calculated near-field intensity distribution $|E|^2$ of (**a**) circular and (**b**) triangular nanopatterns with ϕ, $L = 600$ nm at $\Lambda = 2$ μm. A 5-nm-thick ITO layer was assumed to be deposited on the nanopattern with $\theta_{eva} = 30^\circ$

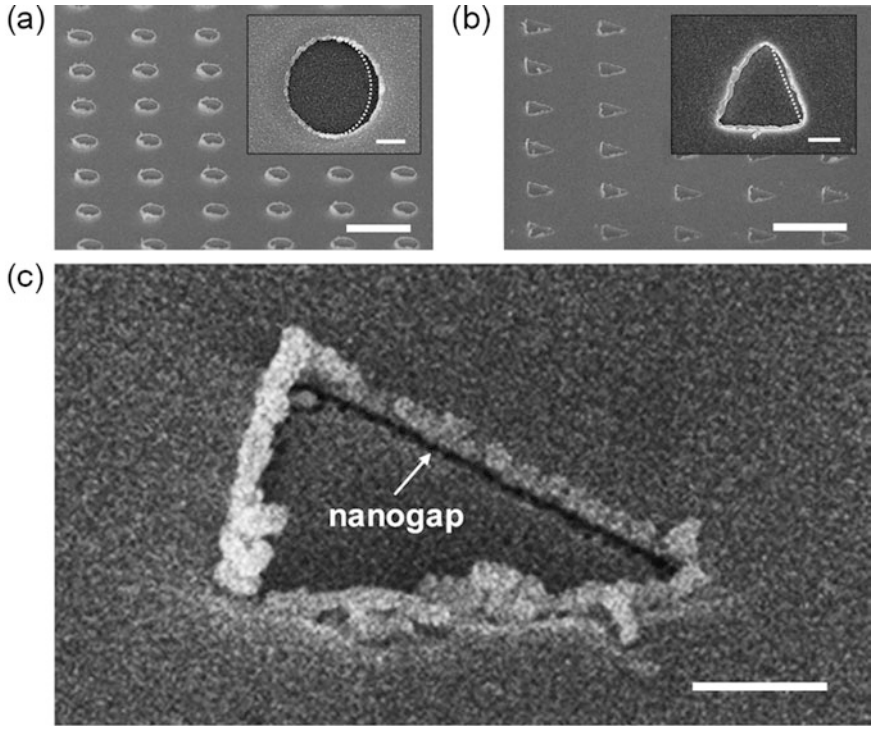

Fig. 6 SEM images: (**a**) circular and (**b**) triangular nanopattern arrays. (**c**) A magnified image of a triangular nanogap pattern. A very narrow nanogap is clearly visible at the side ridge of a triangular nanoaperture. Each inset of (**a**) and (b) shows the nanogap created on a circular and triangular aperture (scale bars: 2 μm for (**a**) and (**b**), 200 nm for (**c**), insets of (**a**) and (**b**))

target binding in the nanogap. Nonspecific binding that may be present is estimated to be insignificant.

SEM images of fabricated 3D nanogap arrays formed on circular and triangular patterns were presented in Fig. 6, in which the existence of nanogap at the ridge of nanoaperture can be corroborated. When d_g is fixed, the angle of oblique evaporation affects the underlying nanogap size, which is directly related to the amount of target molecules, i.e., DNA immobilization and eventually hybridization. Each colocalization area of experimentally fabricated circular and triangular nanopatterns was estimated from the SEM images in Fig. 6a, b to be 24,600 ± 7000 and 19,300 ± 4600 nm^2 without considering the sidewall area of the apertures. This is in good agreement with the numerically estimated gap area (*see* **Note 4**).

(a) Before immobilization of p-DNAs, first, sample chips were cleaned in acetone for 5 min and in ethanol.

(b) The sample chip surface was treated in plasma cleaner (Harrick Scientific Products, Pleasantville, NY).

3.5 Experimental Measurements of DNA Hybridization

3.5.1 DNA Preparation

(c) 1 ml Phosphate buffered saline (PBS) buffer (pH = 7.4) including 4 μM thiol hexane labeled probe ssDNA (HSssDNA) was injected to flow channel by a sylinge pump. The sample chip was immersed in the buffer at 4 °C for 4 h to immobilize the p-DNAs at surface (*see* **Note 5**). In order to obtain SPR angle shift, the reference SPR angle was measured and smoothed by 50th order Fourier filter.

(d) For DNA hybridization, PBS buffer including 4 μM t-DNAs was injected on the p-DNA-immobilized sample chip surface for 120 min by a fluidic channel of a micropump (KD Scientific, Holliston, MA) at a volume flow rate of 150 μL/hr. The sample chip was incubated to improve the efficiency of hybridization through mild heating. For 2 h, the solution of t-DNAs is warmed to 65 °C and slowly cooled down to room temperature. Finally, the SPR angle shift was obtained by comparing SPR angles before and after the DNA hybridization.

SPR shifts were measured using linear nanogratings and 3D nanopattern arrays to analyze the sensor performance, as shown in Figs. 7 and 8 for DNA hybridization. Two metrics were set to evaluate the sensor performance: (1) sensitivity enhancement factor, i.e., resonance shift with respect to the shift obtained from conventional SPR detection, and (2) molecular binding capacity measured by colocalization in the nanogap.

3.5.2 Sensitivity Enhancement

First, resonance angle shifts were measured based on colocalization using plasmonic nanogap arrays, such as nanogratings, circular and triangular nanopatterns, compared to non-colocalized SPR detection without nanogap structures. In the non-colocalized detection, DNA hybridization occurs on the overall metal surface of nanostructures. This leads to inefficient detection of target molecules, majority of which may be distributed in the region with weak near-fields.

Figure 7a shows raw data of measured SPR angle shifts θ_{SPR} in various platforms. In case of non-colocalized detection, resonance angle shifts made on nanostructures were detected to be slightly larger than that of the thin film control. The larger resonance shift is associated with the increase of the total area available for DNA hybridization due to the presence of nanopatterns. For colocalized detection, SPR angle shift tends to be larger with an increase of the ITO-evaporation angle (θ_{eva}). A larger θ_{eva} enlarges the nanogap surface area, which allows more probe-DNAs (p-DNAs) to immobilize at the nanogap surface. Increased resonance shifts were observed for colocalization by nanogratings because the nanogap area by grating patterns is much larger than that of 3D nanogap patterns and therefore induces more p-DNA targets to participate in hybridization.

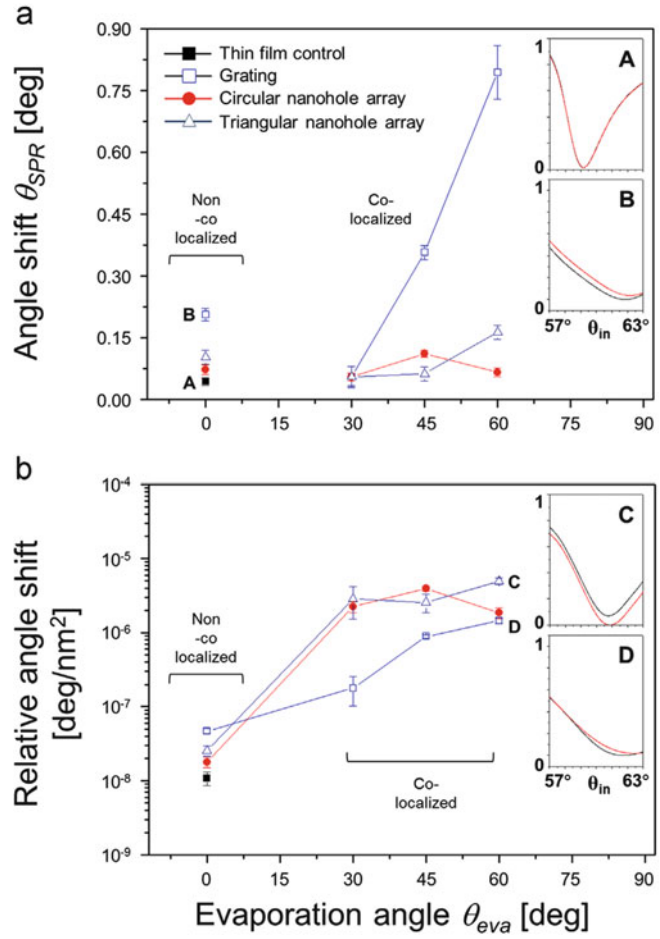

Fig. 7 (**a**) Measured SPR angle shifts as the evaporation angle (θ_{eva}) varies. (**b**) Relative angle shifts (*RAS*) after normalization by the nanogap area. Reproduced from Y. Oh et al. 2014 with permission from Elsevier

The angular shift made of 3D nanogap patterns may not be clear in Fig. 7a. To consider the total area of nanogap to which target molecules can bind for biomolecular interactions, a new parameter was introduced as the resonance shift normalized by the amount of molecular interactions, i.e., *relative angle shift (RAS)* = θ_{SPR}/*nanogap area*, where the amount of molecular interactions is presumed to be proportionate to the nanogap area. Mearsured *RAS*, corresponding to each case in Fig. 7a, is presented in Fig. 7b. First, RAS_{3D} increases by more than two orders based on colocalization with 3D nanogap structures such as circular and triangular patterns, compared to *RAS* of the non-colocalized control. In the case of using 2D grating-based nanogap arrays, RAS_{2D} is increased by one order of magnitude. Colocalization by 3D triangular patterns produces the maximum RAS_{3D} at $\theta_{eva} = 60°$,

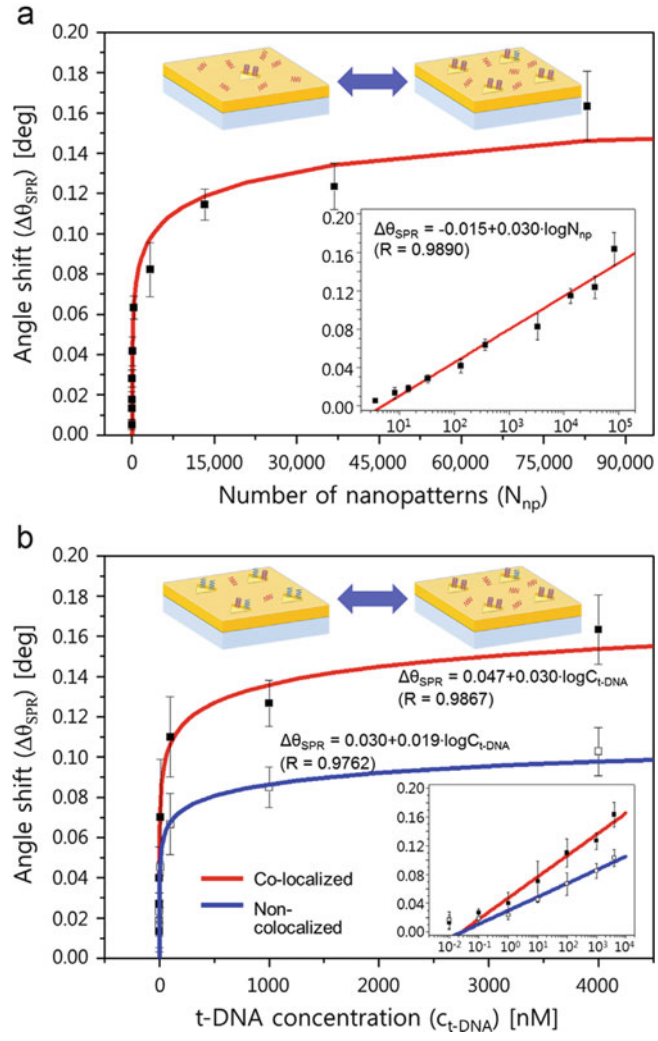

Fig. 8 (**a**) Angular SPR shifts ($\Delta\theta_{SPR}$) measured as the array period (Λ) is varied. 3D nanogap arrays were created by triangular nanopatterns at $\theta_{eva} = 60^{\circ}$ and the concentration of t-DNA was fixed at 4 μM. Inset shows a linear relation between $\Delta\theta_{SPR}$ and log(N_{np}). (**b**) Angular shifts measured as the concentration of t-DNAs ($C_{t\text{-}DNA}$) varied with the fixed p-DNA concentration at 4 μM. *Inset* also shows a linear relation between $\Delta\theta_{SPR}$ and log($C_{t\text{-}DNA}$). Reproduced from Y. Oh et al. 2014 with permission from Elsevier

which is 460 times larger than non-colocalized *RAS* measured at thin film control. The result is associated with efficient localization of SP at triangular nanopatterns as well as reduced nanogap area that is optimized to the size of localized fields [18, 19]. Note that the optimum evaporation angle for 3D nanogap arrays is not directly proportional to the nanogap area. The evaporation angle θ_{eva} may also affect the peak near-field intensity. The insets of Fig. 7.

show the resonance characteristics: A and B for non-colocalized detection, C and D for nanogap-based colocalization. Compared to the insets A, B, and D, 3D nanogap arrays presented in the inset C keep the SPR curve from broadening due to lower plasmonic damping and longer array period.

3.5.3 Molecular Binding Capacity

To evaluate molecular binding capacity as the sensor performance, Fig. 8 shows the isotherm characteristics measured in two ways using the optimum triangular nanogap arrays in 3D at $\theta_{eva} = 60^{\circ}$, which was determined to produce the maximum *RAS* as shown in Fig. 7b. First, the array period was increased when the concentration of target DNA was fixed as 4 μM, which in effect decreases the concentration of probe DNA. Secondly, the isotherm characteritic was also measured by varying the concentration when the array period and the concentration of probe DNA were fixed at 2 μm and 4 μM respectively.

To extract the detection sensitivity of colocalized SPR sensing based on 3D nanogaps, resonance angle shifts ($\Delta\theta_{SPR}$) were measured by varying the array period as shown in Fig. 8a, where the amount of probe DNA is gradually reduced with an increase of array period while the amount of target DNA remains constant. The relation between $\Delta\theta_{SPR}$ and the number of nanopatterns (N_{np}) was presented as

$$\Delta\theta_{SPR} = -0.015 + 0.030 \log N_{np}. \quad (5)$$

In Eq. 5, $\Delta\theta_{SPR}$ is proportional to $\log(N_{np})$, which means SPR shifts are linearly increased when the amount of p-DNA is exponentially increased. As N_{np} is reduced, the detection and the nature of resonance angle shifts change from being target-limited to probe-limited with transition taking place at $N_{np} = 3300\sim13{,}000$ ($\Lambda = 5$–10 μm), i.e., the limit of detection arises in the probe-limited detection of DNA hybridization. If we assume surface probe density to be 4×10^{12} molecules/cm^2 and hybridization efficiency 40%, a total effective nanogap area of 264,000 nm^2 in a 650-μm-diameter beam spot measures approximately 4200 molecules. This corresponds to the molecular binding capacity of 1.6 fg/mm^2 based on the molecular weight of 7.4 kDa for a 24-mer t-DNA. The results suggest that the detection sensitivity of 3D nanogap-based SPR sensing, compared to that of conventional SPR sensors, should be improved by more than three orders of magnitude.

Figure 8b shows the measured angular shifts when the concentration of target DNAs ($C_{t\text{-}DNA}$) was varied. In this case, p-DNA concentration was fixed at 4 μM and other conditions remained the same as in Fig. 8a. Surprisingly, the relation between $\Delta\theta_{SPR}$ and $C_{t\text{-}DNA}$ is similar to what was measured from $\Delta\theta_{SPR}$ and N_{np}, which implies that the amount of DNA hybridization is limited by

p-DNAs (N_{np}) or t-DNAs ($C_{t\text{-}DNA}$). On condition that a much smaller number of DNAs participate in hybridization, 160% of enhancement was measured based on the slope in the inset $\Delta\theta_{SPR}/\log(C_{t\text{-}DNA})$.

4 Notes

1. Overall procedure was automatically controlled by computer. The size of a measurement chamber is roughly 10 mm (L) × 1.5 mm (W) × 0.5 mm (D), and ambient temperature was maintained at 19.6 ± 0.2 °C for measurement stability.
2. Two concentric motorized rotation stages were employed to implement angle-scanning of $\theta/2\theta$ measurement. The motorized rotation stages were controlled with a minimum motion increment of 0.0002°, absolute accuracy of 0.008°, uni-directional repeatability of 0.001°, and wobble at 20 μrad.
3. ITO provides chemical and optical stability to SPR sensors in terms of material degradation [20]. During the evaporation, chamber temperature was maintained at 200 °C to enhance adhesion by annealing.
4. The area of nanogap produced by a circular (triangular) nanoaperture with ϕ (L) = 600 nm and d_g = 20 nm was numerically calculated as listed in the table at 2-μm array period, i.e., a unit area of 2 × 2 μm^2. For 2D gratings, the array period was 400 nm. Area unit is nm^2.

θ_{eva}	2D grating	3D circular aperture	3D triangular aperture
30°	320,000	24,000	19,000
45°	400,000	28,000	24,000
60°	550,000	35,000	33,000

5. The estimated surface density of immobilized p-DNA is 4.0×10^{12} molecules/cm^2 [21].

References

1. Kim D (2005) Effect of the azimuthal orientation on the performance of grating-coupled surface-plasmon resonance biosensors. Appl Optics 44:3218–3223
2. Campbell CT, Kim G (2007) SPR microscopy and its application to high-throughput analyses of biomolecular binding events and their kinetics. Biomaterials 28:2380–2392
3. Dasary SSR, Singh AK, Senapati D, Yu H, Ray PC (2009) Gold nanoparticle based label-free SERS probe for ultrasensitive and selective detection of trinitrotoluene. J Am Chem Soc 131:13806–13812
4. Vollmer F, Arnold S (2008) Whispering-gallery-mode biosensing: label-free detection down to single molecules. Nat Methods 5:591–596

5. Oh Y, Lee W, Kim Y, Kim D (2014) Self-aligned colocalization of 3D plasmonic nanogap arrays for ultra-sensitive surface plasmon resonance detection. Biosens Bioelectron 51:401–407
6. Byun KM, Kim S, Kim D (2005) Design study of highly sensitive nanowire-enhanced surface plasmon resonance biosensors using rigorous coupled wave analysis. Opt Express 13:3737–3742
7. Kim K, Yoon SJ, Kim D (2006) Nanowire-based enhancement of localized surface plasmon resonance for highly sensitive detection: a theoretical study. Opt Express 14:12419–12431
8. Moon S, Kim Y, Oh Y, Lee H, Kim HC, Lee K, Kim D (2012) Grating-based surface plasmon resonance detection of core-shell nanoparticle mediated DNA hybridization. Biosens Bioelectron 32:141–147
9. Yu H, Kim K, Ma K, Lee W, Choi JW, Yun CO, Kim D (2013) Enhanced detection of virus particles by nanoisland-based localized surface plasmon resonance. Biosens Bioelectron 41:249–255
10. Hoa XD, Kirk AG, Tabrizian M (2009) Enhanced SPR response from patterned immobilization of surface bioreceptors on nano-gratings. Biosens Bioelectron 24:3043–3048
11. Ma K, Kim DJ, Kim K, Moon S, Kim D (2010) Target-localized nanograting-based surface plasmon resonance detection toward label-free molecular biosensing. IEEE J Sel Topics Quantum Electron 16:1004–1014
12. Kim Y, Chung K, Lee W, Kim DH, Kim D (2012) Nanogap-based dielectric-specific colocalization for highly sensitive surface plasmon resonance detection of biotin-streptavidin interaction. Appl Phys Lett 101:233701
13. Yang H, Lee W, Hwang T, Kim D (2014) Probabilistic evaluation of surface-enhanced localized surface plasmon resonance biosensing. Opt Express 22:28412–28426
14. Ryu Y, Moon S, Oh Y, Kim Y, Lee T, Kim DH, Kim D (2014) Effect of coupled graphene oxide on the sensitivity of surface plasmon resonance detection. Appl Optics 53:1419–1426
15. Chung K, Rani A, Lee J-E, Kim JE, Kim Y, Yang H, Kim SO, Kim D, Kim DH (2015) A systematic study on the sensitivity enhancement in graphene plasmonics sensors based on layer-by-layer self-assembled graphene oxide multilayers and their reduced anologues. ACS Appl Mater Interfaces 7:144–151
16. Kubatkin S, Danilov A, Hjort M, Cornil J, Brédas J-L, Stuhr-Hansen N, Hedegård P, Bjørnholm T (2003) Single-electron transistor of a single organic molecule with access to several redox states. Nature 425:698–701
17. Elhadj S, Singh G, Saraf RF (2004) Optical properties of an immobilized DNA monolayer from 255 to 700 nm. Langmuir 20:5539–5543
18. Fromm DP, Sundaramurthy A, Schuck PJ, Kino G, Moerner WE (2004) Gap-dependent optical coupling of single "bowtie" nanoantennas resonant in the visible. Nano Lett 4:957–961
19. Haes AJ, Zou S, Schatz GC, Van Duyne RP (2004) Nanoscale optical biosensor: short range distance dependence of the localized surface plasmon resonance of noble metal nanoparticles. J Phys Chem B 108:6961–6968
20. Szunerits S, Castel X, Boukherroub R (2008) Surface plasmon resonance investigation of silver and gold rilms coated with thin indium tin oxide layers: Influence on stability and sensitivity. J Phys Chem C 112:15813–15817
21. Steel AB, Herne TM, Tarlov MJ (1998) Electrochemical quantitation of DNA immobilized on gold. Anal Chem 70:4670–4677

http://www.springer.com/978-1-4939-6846-6

Biosensors and Biodetection
Methods and Protocols Volume 1: Optical-Based Detectors
Rasooly, A.; Prickril, B. (Eds.)
2017, XXIII, 456 p. 179 illus., 142 illus. in color.,
Hardcover
ISBN: 978-1-4939-6846-6
A product of Humana Press